

RAANet: Range-Aware Attention Network for LiDAR-based 3D Object Detection with Auxiliary Density Level Estimation

Yantao Lu*
Syracuse University

ylu25@syr.edu

Weiheng Chai
Syracuse University

wchai01@syr.edu

Xuetao Hao*
Didi Labs

xuetaoha@alumni.usc.edu

Muchenxuan Tong
Didi Labs

tongmuchenxuan@didiglobal.com

Shiqi Sun
Duke University

shiqi.sun@duke.edu

Senem Velipasalar
Syracuse University

svelipas@syr.edu

Abstract

3D object detection from LiDAR data for autonomous driving has been making remarkable strides in recent years. Among the state-of-the-art methodologies, encoding point clouds into a bird’s-eye view (BEV) has been demonstrated to be both effective and efficient. Different from perspective views, BEV preserves rich spatial and distance information between objects; and while farther objects of the same type do not appear smaller in the BEV, they contain sparser point cloud features. This fact weakens BEV feature extraction using shared-weight convolutional neural networks. In order to address this challenge, we propose Range-Aware Attention Network (RAANet), which extracts more powerful BEV features and generates superior 3D object detections. The range-aware attention (RAA) convolutions significantly improve feature extraction for near as well as far objects. Moreover, we propose a novel auxiliary loss for density estimation to further enhance the detection accuracy of RAANet for occluded objects. It is worth to note that our proposed RAA convolution is lightweight and compatible to be integrated into any CNN architecture used for the BEV detection. Extensive experiments on the nuScenes dataset demonstrate that our proposed approach outperforms the state-of-the-art methods for LiDAR-based 3D object detection, with real-time inference speed of 16 Hz for the full version and 22 Hz for the lite version. The code is publicly available at an anonymous Github repository <https://github.com/anonymous0522/RAANet>.

1. Introduction

With rapid improvement of processing units, and thanks to the extraordinary success of deep neural networks, the perception of autonomous driving has been flourishing in recent years. 3D object detection from LiDAR sensors

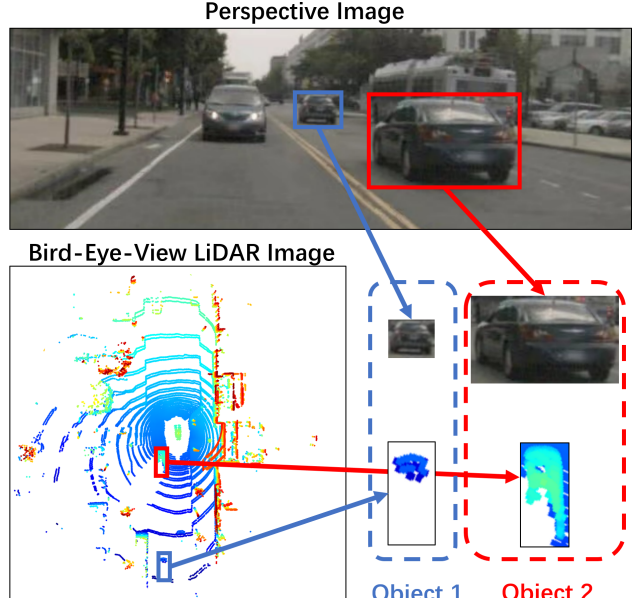


Figure 1. **Motivation.** Different from camera images with perspective distortion, in BEV, objects that are farther from the ego-vehicle do not appear in smaller sizes, but contain sparser set of LiDAR points instead. Thus, an object in BEV may appear different depending on the distance of the object to ego-vehicle, which weakens BEV feature extraction using shared-weight CNNs.

is one of the important capabilities for autonomous driving. Early works employ 3D convolutional neural networks, which have slow processing speeds and large memory requirements. In order to decrease the memory requirements and provide real-time processing, recent methodologies leverage voxelization and bird’s-eye view (BEV) projection. Voxelization is widely implemented as a prepossessing method for 3D point clouds due to the computing efficiency, provided by more structured data, and performance accuracy [10] [33] [32] [25]. In general, voxeliza-

*Equal contribution

tion divides a point cloud into an evenly spaced grid of voxels, and then assigns 3D LiDAR points to their respective voxels. The output space preserves the Euclidean distance between objects and avoids overlapping of bounding boxes. This fact keeps object size variation in a relatively small range, regardless of their distance from the LiDAR, which benefits the shape regression during training. However, as shown in Figure 1, the voxels that are farther away from the ego-vehicle contain significantly fewer LiDAR points than the near ones. This leads to a situation where different representations may be extracted for an object at different distances to the ego-vehicle. In contrast to perspective view, where feature elements are location-agnostic, BEV feature maps are location sensitive. Thus, different convolutional kernel weights should be applied to feature elements at different locations of the feature map. In other words, location information should be introduced to the feature maps, and the convolutional kernels should be adjustable to the location information of corresponding feature maps.

In this paper, we propose Range-Aware Attention Network (RAANet), which contains novel Range-Aware Attention Convolutional layer (RAAConv) designed for object detection from LiDAR BEV. RAAConv is composed of two independent convolutional branches and attention maps, which is sensitive to the location information of the input feature map. Our approach is inspired by properties of BEV images, which are illustrated in Fig. 1. Points get more sparse as the distance between an objects and ego-vehicle increases. Ideally, for BEV feature maps, elements at different locations should be processed by different convolution kernels. However, applying different kernels will significantly increase the computational expense. In order to utilize the location information during BEV feature extraction, while avoiding heavy computation at the same time, we regard a BEV feature map as a composition of sparse features and dense features. We apply two different convolution kernels to simultaneously extract sparse and dense features. Each extracted feature map has half the channel size of the final output. Meanwhile, range and position encodings are generated based on the input shape. Then, each range-aware attention heatmap is computed from the corresponding feature map and the range and position encodings. Finally, the attention heatmaps are applied on the feature maps to enhance feature representation. The feature maps generated from two branches are concatenated channel-wisely as the RAAConv output. Details are presented in Sec. 3.2.

In addition, the effect of occlusion on the LiDAR data cannot be ignored, since an object can have different point distributions under different amounts of occlusion. Thus, we propose an efficient auxiliary branch, referred to the Auxiliary Density Level Estimation Module (ADLE), allowing RAANet to take occlusion into consideration. Since annotating various occlusions is a time consuming and ex-

pensive task, instead of estimating an occlusion instance, we design the ADLE to estimate a density level for each object. If there is no occlusion, the point density levels for near objects are higher than those of far objects. However, if a near object is occluded, its point density level decreases. Therefore, by combining range information and density level information, we are able to simulate the occlusion information. ADLE is only used in the training stage for providing density information guidance, and can be removed in inference state for computational efficiency.

Contributions. The main contributions of this work include the following:

- We propose the RAAConv layer, which allows LiDAR-based detectors to extract more representative BEV features. In addition, RAAConv layer can be integrated into any CNN architecture used for LiDAR BEV.
- We propose a novel auxiliary loss for density estimation to help the main network learn occlusion related features. This proposed density level estimator further enhances the detection accuracy of RAANet on occluded objects as well.
- We propose the Range-Aware Attention Network (RAANet), which integrates the aforementioned RAA and ADLE modules. RAANet is further optimized by generating anisotropic Gaussian heatmap based on the ground truth, which is introduced in Sec. 3.4.
- The code is available at an anonymous GitHub repo. [1].

2. Related Work

In recent years, many methods have been presented advancing the field of 3D object detection. Pixor [27] performs the voxelization via a customized encoding algorithm of the point clouds. However, the hand-craft design of voxelization limits the generalization and adaptation of Pixor. Hence, to overcome this shortcoming, VoxelNet [33] proposes a PointNet and 3D convolutional layer to voxelize the points clouds autonomously. Compared to VoxelNet, SEC-OND [26] improves the inference time with the sparsely embedded convolutional layers. Although VoxelNet-based methodologies provide powerful encoding schemes of point clouds, researchers are still exploring new effective methods. In particular, PointPillar [10] discards 3D convolutional layers and voxelization, and presents a new encoding scheme called pillar. They merge the points of z-axis and then project them into BEV space. Therefore, the points could be processed by 2D convolutions. They propose an end-to-end pipeline with only 2D convolutional layers based on pillars, which significantly improves the processing speed.

The aforementioned studies have provided effective and fast methodologies to encode point clouds. However, how to effectively process these encodings and perform precise bounding box regression still remains to be explored further.

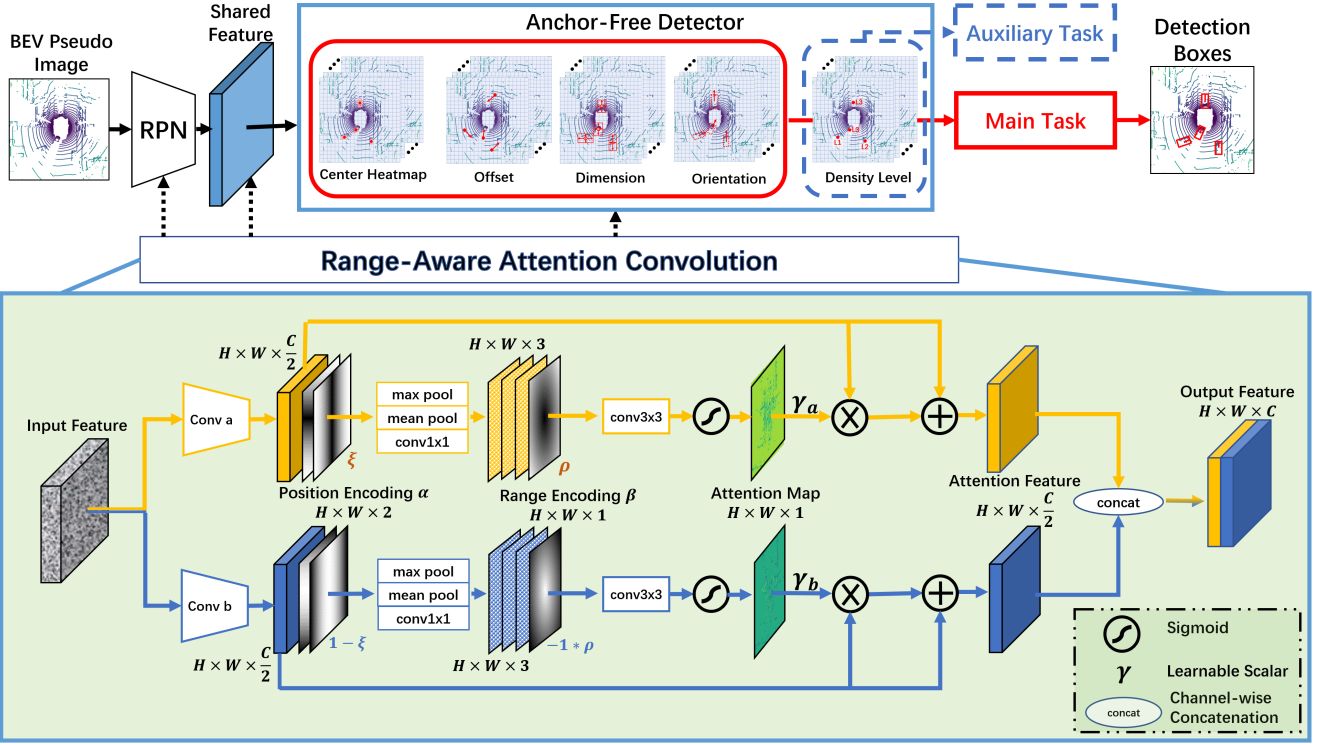


Figure 2. **Overview of the proposed network.** The RPN is designed to extract the shared feature from a BEV pseudo image. Then, the main detection heads and an auxiliary density estimation head are appended. The auxiliary head only exists during training and is omitted during inference. Finally, 3D bounding boxes are obtained from the main heads. Our proposed RAACConv layer, illustrated in the lower part of the figure, replaces the original Conv2D layer. In general, this layer contains two branches, and each branch applies position and range encodings to generate its range-aware attention heatmap. Then, extracted features in each branch are enhanced by the heatmap with a residual architecture. Those enhanced features are concatenated for the final output features.

CenterPoint [29] provides a regression method by focusing on the center points of all bounding boxes, and hence reduces the complexity of rotation. Although the rotation invariance of the center point makes this method accurate and fast, significant amount of positional information is lost because of the top-view encoding and the isotropic Gaussian mask. To avoid these drawbacks, a series of works consider the positional information in the feature extractor. Particularly, CBAM [24] adds spatial attention and channel attention modules into the convolutional layers. Although this scheme provides a new insight of adding attention mechanism, it still cannot well encode the complicated spatial information from the LiDAR point clouds. Thus, it is necessary to design a novel convolutional network to utilize the location and density information from the point clouds.

3. Range-Aware Attention Network

3.1. Overview of RAANet

The main architecture of our proposed Range-Aware Attention Network (RAANet) is presented in Fig. 2. We incorporate ideas from CenterNet [31] [29] to build an

anchor-free detector, and also introduce two novel modules: the Range-Aware Attention Convolutional Layer (RAACConv) and the Auxiliary Density Level Estimation Module (ADLE).

RAANet takes the 3D LiDAR points as input and generates a set of 3D oriented bounding boxes as the output. Inspired by CenterPoint [29], we implement a feature extractor with 3D sparse convolutional network to extract the BEV feature map from voxelized point clouds. This resulting feature map is reshaped and formed into a BEV pseudo image, which can be regarded as a multi-channel 2D image. The Region Proposal Network (RPN) takes this BEV pseudo image as input and employs multiple down-sample and up-sample blocks to generate a high-dimensional feature map. In addition to the detection heads in main task, we propose an auxiliary task for density level estimation to achieve better detection performance. Meanwhile, the RAACConv layers are utilized in all convolutional modules shown as Fig. 2. Center probability heatmap is generated from one of the detector heads, and maximums in local neighborhoods are treated as the centers of ground-truth bounding boxes (bbox). The regression of bbox attributes,

including offsets, dimensions and orientations, are computed from the other heads in the main detection task. Parallel to the main task, the proposed ADLE, as an auxiliary task, estimates density level for each bounding box. In general, ADLE classifies each bounding box into different density levels, based on the number of points in each bbox. ADLE is a portable block for the whole network, i.e. it is employed only in the training process and is not used during inference for higher computational efficiency.

For the training phase, we denote the loss components as the heatmap classification head, bbox regression head and auxiliary density level head as l_{hm} , l_{box} and l_{aux} , respectively. The total loss function of RAANet is formulated as

$$l = l_{hm} + \lambda_{box} l_{box} + \lambda_{aux} l_{aux}, \quad (1)$$

where λ_{box} and λ_{aux} are scalar weights for balancing multi-task loss. l_{hm} and l_{aux} are designed as the penalty-reduced focal losses [12] [31], and l_{box} is designed as the smooth L1 loss.

3.2. Range-Aware Attention Convolutional Layer (RAACconv)

We propose the Range-Aware Attention Convolutional Layer (RAACconv), which, by leveraging the specially designed attention blocks, becomes sensitive to range and position information. This is the major difference between the proposed RAACconv and traditional convolutional layer. RAACconv is employed in the aforementioned RPN and detection heads. As shown in Fig. 2, RAACconv first utilizes two sets of convolutional kernels to extract an intermediate feature map for each branch. Then, the position encodings are generated and embedded into intermediate feature maps. Two range-aware heatmaps are calculated by a series of convolution and pooling operations using the intermediate feature maps and range encodings. More specifically, given an input feature map $I \in \mathbb{R}^{H_{in} \times W_{in} \times C_{in}}$, two separate intermediate feature maps, $\mathbf{F}_a, \mathbf{F}_b \in \mathbb{R}^{H_{out} \times W_{out} \times \frac{C_{out}}{2}}$, are generated by

$$\mathbf{F}_i = \zeta(\mathbf{I}, w_F^i), i \in a, b, \quad (2)$$

where $\zeta(\cdot)$ represents convolution operation and w_F^i denotes the corresponding convolution kernel.

Meanwhile, the position encoding map $\xi \in \mathbb{R}^{H_{out} \times W_{out} \times 2}$ and range encoding map $\rho \in \mathbb{R}^{H_{out} \times W_{out} \times 1}$ are generated from the intermediate feature map \mathbf{F}_a . ξ and ρ are calculated from shape information and do not depend on the values inside the tensor \mathbf{F}_a . There are two components of ξ : row encoding r and column encoding c . ξ and ρ are generated as follows:

$$\begin{aligned} r_{ij} &= \frac{2|i - \frac{H}{2}|}{H}, \quad c_{ij} = \frac{2|j - \frac{H}{2}|}{W} \\ \rho_{ij} &= 2\sqrt{r_{ij}^2 + c_{ij}^2} - 1 \\ s.t. \quad i &\in \{1, 2, \dots, H\}, \quad j \in \{1, 2, \dots, W\} \end{aligned} \quad (3)$$

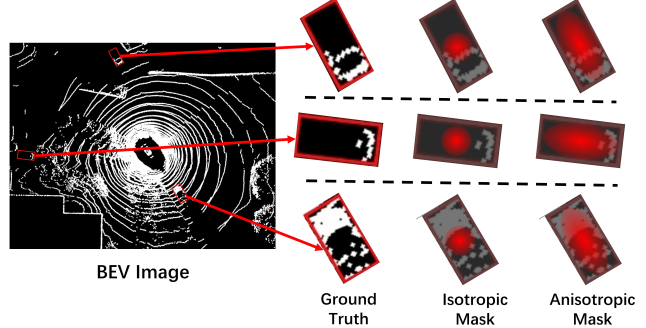


Figure 3. **Illustration of Anisotropic 2D Gaussian Mask.** Traditional Isotropic Gaussian Mask neglects the rotation of the rectangular bounding box. We propose an Anisotropic 2D Gaussian Mask, allowing the mask to better fit for the ground truth. The Anisotropic mask is able to introduce the heading angle information, which is beneficial to bbox regression as well.

Values of r, c are bounded in $[0, 1]$. Values of ρ are bounded in $[-1, 1]$.

Since the proposed network is designed by using two convolution kernels to extract dense and sparse features separately, we append ξ to intermediate feature map \mathbf{F}_a channel-wise, and reversely append $1 - \xi$ to \mathbf{F}_b . The generated features are denoted as \mathbf{F}'_a and \mathbf{F}'_b . Maximum pooling, mean pooling and 1×1 conv2D are applied on \mathbf{F}'_a and \mathbf{F}'_b separately to obtain the spatial embeddings \mathbf{F}^ξ_a and \mathbf{F}^ξ_b . Then, similar to positional appending, the range encoding map ρ is appended to \mathbf{F}^ξ_a , and $-\rho$ is appended to \mathbf{F}^ξ_b . The appended features are processed by a 3×3 conv2D layer followed by sigmoid activation to obtain the range-aware attention heatmaps \mathbf{f}_a and \mathbf{f}_b . The heatmaps \mathbf{f}_a and \mathbf{f}_b are then multiplied by learnable scalars γ_a and γ_b separately. γ_a and γ_b are initialized as 1.0 and gradually learn the weights during training [30]. The output feature maps \mathbf{F}''_a and \mathbf{F}''_b are calculated from $\mathbf{F}'_a, \mathbf{f}_a, \gamma_a$, and $\mathbf{F}'_b, \mathbf{f}_b, \gamma_b$ using a residual connection, which is defined as:

$$\mathbf{F}''_i = (\gamma_i \mathbf{f}_i) \otimes \mathbf{F}'_i + \mathbf{F}'_i, \quad i \in a, b \quad (4)$$

where \otimes is the operation performing channel-wise stacking and element-wise multiplication. The final output for RAACconv is the channel-wise concatenation of \mathbf{F}''_a and \mathbf{F}''_b , which has size of $H_{out} \times W_{out} \times C_{out}$.

In addition, we customize the initialization of convolutional kernel weights, which are only related to the range encoding channel, as absolute values of the original initialization. The reason is that ρ is normalized within $[-1, 1]$. It is demonstrated by an ablation study that the aforementioned initialization method can improve the average precision (AP) performance of the RAANet.

It is worth noting that the proposed RAACconv can be readily plugged in any convolutional network for LiDAR BEV detection.

3.3. Auxiliary Density Level Estimation Module (ADLE)

The Auxiliary Density Level Estimation Module (ADLE) is an additional classification head that is parallel to the main detection heads. The ADLE indicates density level for each bbox. In general, we design ADLE to estimate the number of LiDAR points inside a detected bbox. We have empirically found that this estimation is straightforward yet helpful to the detector. Moreover, instead of making ADLE perform a precise value regression, we divide the number of points into three density bins and let ADLE perform a classification task, which is more achievable. More specifically, we divide the point density level into three bins: sparse (label 1), adequate (label 2) and dense (label 3). We have statistically analyzed the distribution of the number of points and employed two thresholds T_0^i, T_1^i to determine the density level for each object class i . The three density levels are defined as:

$$D_i(n) = \begin{cases} 1, & \text{if } n < T_0^i \\ 2, & \text{if } T_0^i \leq n < T_1^i \\ 3, & \text{if } n \geq T_1^i \end{cases} \quad (5)$$

where n denotes the number of points, and D_i represents the density level for the i -th class. As shown in Fig. 3, with no occlusion, objects near the ego-vehicle have high point density levels and faraway objects have low density levels. However, when an object is occluded, the density level will be lower than the unoccluded case at the same distance. Since we incorporate position and range information into RAACconv, ADLE is able to further help RAANet extract occlusion information by estimating the point density levels instead of the actual occlusion severity, which is hard to annotate from the ground truth.

3.4. Anisotropic Gaussian Mask

Anisotropic Gaussian Mask represents the centerness probability for each position in an annotated bbox. The centerness heatmap is generated as the ground truth for the classification head. In this work, we propose an Anisotropic Gaussian Mask, shown in Fig. 3, as the method of 2D Gaussian distribution generation, to be used for the centerness probabilities of a given oriented bbox. More specifically, the Gaussian distribution $N(\mu, \Sigma)$ is designed in anisotropic way: the σ values for the 2 dimensions, denoted as σ_0, σ_1 , which are the diagonals of Σ , are different, and their values are determined from the length and width of the bbox, respectively. The procedure of generating the center heatmap, denoted by \mathfrak{M} , can be formulated as:

$$\mathfrak{M}_{C_H, C_W, H, W, s}(x, y) = \mathbb{1}_{\mathfrak{B}}(N_{\mu, \Sigma}(x, y)) \quad (6)$$

where,

$$\begin{aligned} \mathfrak{B} &= \{x \in [C_W - \frac{W}{2}, C_W + \frac{W}{2}] \cap y \in [C_H - \frac{H}{2}, C_H + \frac{H}{2}]\} \\ \mu &= [C_W, C_H]^T \\ \Sigma &= \begin{bmatrix} W/d_{cls} & 0 \\ 0 & H/d_{cls} \end{bmatrix} \end{aligned} \quad (7)$$

and (C_H, C_W) and (H, W) denote the center location and dimensions of a bbox, respectively. s indicates the ground truth class for the bbox. $\mathbb{1}(\cdot)$ is the indicator function and \mathfrak{B} denotes the set of locations that are inside the bbox. d_{cls} is a decay factor that decides the sharpness of generated heatmap. The value of d_{cls} depends on the class of the given bbox.

3.5. Loss Functions

Following Eq. (1), the center heatmap loss L_{hm} is defined as:

$$L_{hm} = -\frac{1}{N} \sum_{\hat{p}} \{(1-h)^\alpha \log(h) I_{\hat{h}>1-\epsilon} + (1-\hat{h})^\beta h^\alpha \log(1-h) I_{\hat{h}<1-\epsilon}\}, \quad (8)$$

where h and \hat{h} are the predicted and ground-truth heatmap values, respectively. ϵ is a small value for numerical stability. α and β are the parameters to control penalty-reduced focal loss. For all the experiments, we follow the setting in [19]: $\epsilon = 1e-3$, $\alpha = 2$ and $\beta = 4$.

The bounding box head is responsible for location, dimension and orientation regression, which are represented by the following parameters: $\Gamma = [\delta_x, \delta_y, \delta_z, l, w, h, \theta]$, where $\delta_x, \delta_y, \delta_z$ are the box center offsets with respect to the corresponding voxel centers; and l, w, h and θ denote the length, width, height and yaw of a bounding box. We apply smoothed L1 (SL1) losses to regress $\sin(\theta)$ and $\cos(\theta)$ for the θ attribute, and directly regress actual values for other attributes:

$$L_{\theta_i} = SL1(\sin(\theta_i) - \sin(\hat{\theta}_i)) + SL1(\cos(\theta_i) - \cos(\hat{\theta}_i)) \quad (9)$$

$$L_{\Gamma_i \setminus \theta} = SL1(\Gamma_i \setminus \theta - \hat{\Gamma}_i \setminus \hat{\theta}) \quad (10)$$

where, $\hat{\cdot}$ denotes ground truth values corresponding to original symbols. The total loss for box regression is:

$$L_{box} = \frac{\mathbb{1}_i}{N} \sum_i (L_{\theta_i} + L_{\Gamma_i \setminus \theta}), \quad (11)$$

where N is the number of box samples and $\mathbb{1}_i$ equals 1 if the ground truth heatmap value of the i th feature map pixel is larger than a threshold τ , which is set to 0.2 in the experiments.

	Car	Truck	Bus	Trailer	Cons. Veh.	Ped.	M.cyc.	Bicycle	Traffic Cone	Barrier	mAP
PointPillars [20] [10]	0.760	0.310	0.321	0.366	0.113	0.640	0.342	0.140	0.456	0.564	0.401
SA-Det3D [2]	0.812	0.438	0.572	0.478	0.113	0.733	0.321	0.079	0.606	0.553	0.470
InfoFocus [21]	0.779	0.314	0.448	0.373	0.107	0.634	0.290	0.061	0.465	0.478	0.395
CyliNetRG-single [15]	0.850	0.502	0.569	0.526	0.191	0.843	0.586	0.298	0.791	0.690	0.585
SARPNET [28]	0.599	0.187	0.194	0.180	0.116	0.694	0.298	0.142	0.446	0.383	0.324
PanoNet3D [7]	0.801	0.454	0.540	0.517	0.151	0.791	0.531	0.313	0.719	0.629	0.545
PolarStream [6]	0.809	0.381	0.471	0.414	0.195	0.802	0.614	0.299	0.753	0.640	0.538
MEGVII [34]	0.811	0.485	0.549	0.429	0.105	0.801	0.515	0.223	0.709	0.657	0.528
PointRCNN [17] [16]	0.810	0.472	0.563	0.510	0.141	0.766	0.422	0.134	0.667	0.614	0.510
SSN-v2 [35]	0.824	0.418	0.461	0.480	0.175	0.756	0.489	0.246	0.601	0.612	0.506
ReconfigPP-v2 [22]	0.758	0.272	0.395	0.380	0.065	0.625	0.152	0.002	0.257	0.349	0.325
ReconfigPP-v3 [22] [23]	0.814	0.389	0.430	0.470	0.153	0.724	0.449	0.226	0.583	0.614	0.485
HotSpotNet-0.1m [5]	0.831	0.509	0.564	0.533	0.230	0.813	0.635	0.366	0.730	0.716	0.593
MDetection3D [8]	0.847	0.490	0.541	0.528	0.216	0.793	0.560	0.387	0.714	0.674	0.575
CenterPoint [29]	0.852	0.535	0.636	0.560	0.200	0.846	0.595	0.307	0.784	0.711	0.603
CenterPoint-R [11]	0.854	0.539	0.614	0.575	0.203	0.845	0.591	0.329	0.784	0.706	0.604
CVCNet-single [4]	0.827	0.461	0.458	0.467	0.207	0.810	0.613	0.343	0.697	0.699	0.558
CVCNet-ens [4]	0.826	0.495	0.594	0.511	0.162	0.830	0.618	0.388	0.697	0.697	0.582
RAANet-lite (Ours)	0.858	0.543	0.634	0.552	0.235	0.855	0.620	0.319	0.789	0.740	0.615
RAANet (Ours)	0.860	0.546	0.636	0.553	0.237	0.856	0.633	0.340	0.794	0.749	0.620

Table 1. **Comparison with the state-of-the-art models** for 3D detection on the nuScenes test dataset. We show AP scores for each class and overall mAP scores. Best results are marked in **bold** and 2nd best results are marked in **blue** color. The RAANet refers to the network that implements RAAConv layers for all modules. The RAANet-lite refers to the network that only uses RAAConv layers in the detection heads.

4. Experiments

We introduce the implementation details of the RAANet and evaluate its performance in multiple experiments. The inference results are uploaded to and evaluated by the nuScenes official benchmark [13]. The diagnostic analysis of each component is shown in the ablation studies.

4.1. NuScenes Dataset

We primarily perform the evaluation on the nuScenes dataset [3], which is a public, large-scale and challenging dataset for autonomous driving developed by the team at nuTonomy. The full dataset includes approximately 390k LiDAR sweeps and 1.4M object bounding boxes in 40k key frames. The dataset contains 1000 scenes in total and is splitted as 700 for training, 150 for validation and 150 for testing. There are a total of 10 classes: {car, truck, bus, trailer, construction vehicle, traffic cone, barrier, motorcycle, bicycle, pedestrian}. The scenes of 20 sec. length are manually selected to show a diverse and interesting set of driving maneuvers, traffic situations and unexpected behaviors. The dataset was captured with a 32-channel spinning LiDAR sensor with 360 degree horizontal and -30 to +10 degree vertical FOV. The sensor captures points, which are within 70 meters with ± 2 cm accuracy and returns up to 1.39M points per second.

4.2. Implementation Details

RAANet is implemented in PyTorch framework [14] with anchor-free object detection architecture. All classes are trained together in a single end-to-end network. The weights λ_{box} and λ_{aux} in loss function (Eq. 1) are set to 0.25 and 0.2 respectively. The resolution for voxelization is set to [0.075m, 0.075m, 0.2m] and the voxelization region is $[-54m, 54m] \times [-54m, 54m] \times [-5m, 3m]$. The decay factor d in Sec. 3.4 is set to 3.0 for large size classes (car, truck, bus, trailer, construction_vehicle), to 6.0 for small object classes (traffic_cone, barrier, motorcycle, bicycle, pedestrian). As for the parameters in Sec. 3.5, we set ϵ , α , β and τ to 0.001, 2.0, 4.0 and 0.2, respectively. More details are provided in the configuration file of our anonymous github repository [1]. Two versions of the RAANet are designed in this work: (i) the full version RAANet implements RAAConv layers for all modules; (ii) RAANet-lite version implements RAAConv layers only on the detection heads. Both designs outperform SOTAs. Compared to RAANet, RAANet-lite has faster inference speed, with a small drop on mAP performance.

4.3. Training and Inference

RAANet is trained end-to-end from scratch on $4 \times$ NVIDIA RTX-6000 GPUs. ADAM optimizer [9] with $\beta_1 = 0.9$, $\beta_2 = 0.99$ and One-Cycle learning rate scheduler [18] with maximum $lr = 0.001$ are used during the training. 20 epochs are trained in total and the batch size for each GPU

Model	RAAConv				2D Gaussian	ADLE $\lambda_{aux} = 0.25$	AP (%)	
	Dual Branch	Attention	W. Init	γ			Car	Pedestrian
Baseline	-	-	-	-	-	-	85.23	84.62
+ RAAConv	✓	✗	✗	✗	✗	✗	85.30	84.71
	✗	✓	✗	✗	✗	✗	85.40	84.95
	✓	✓	✗	✗	✗	✗	85.44	85.19
	✓	✓	✓	✗	✗	✗	85.51	85.30
	✓	✓	✓	✓	✗	✗	85.64	85.41
+ 2D Gaussian	✓	✓	✓	✓	✓	✗	85.90	85.42
+ auxiliary loss	✓	✓	✓	✓	✓	✓	86.14	85.64

Table 2. **Ablation study of Range-Aware Attention Network.** Various models are built by different combination of three attributes: RAAConv, Anisotropic Gaussian Mask (2D Gaussian for short) and ADLE. For RAAConv, there are four sub-components: dual branch structure, range-aware attention heatmap, initialization of range-aware kernel weights (Sec. 3.2) and learnable scalar γ (Fig. 2). Baseline is the original CenterPoint [29].

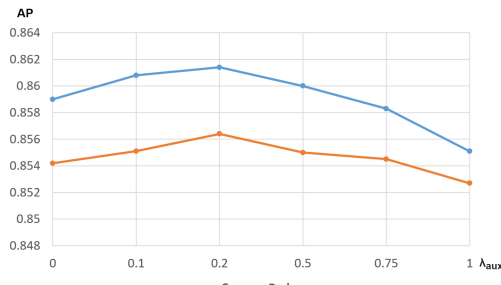


Figure 4. AP results at different loss weights for ADLE (λ_{aux} in Eq. (1)). Experiments are based on the full version RAANet.

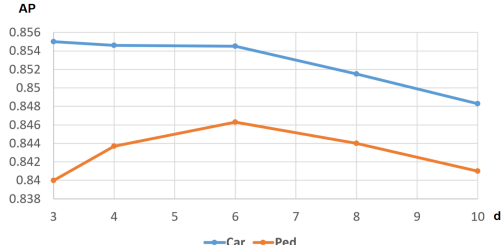


Figure 5. AP results at different Gaussian Σ decay factors, which is denoted as d in Eq. (7). Experiments are based on the baseline.

is set to 4. Random flipping along the x -axis and global rotation around the z -axis, with a random angle sampled from $[-\pi/4, \pi/4]$, are implemented as the augmentation strategies in the training process.

During inference, we reuse the checkpoint with the best mean average precision (mAP) value and evaluate on the official nuScenes evaluation detection metric. The detection score threshold is set to 0.1 and IoU threshold is set to 0.2 for non-maximal suppression. The inference latency for full version of RAANet and RAANet-lite is 62 ms and 45 ms, respectively. Both versions satisfy the real-time 3D detection criteria.

4.4. Results

We present the results, obtained on the test set with both our lite-version and full-version models in Table 1. The architecture of the full version model is illustrated in

Fig. 2. All detection results are evaluated by average precision (AP) for 3D object detection. We choose CenterPoint [29] as the primary baseline for attribute comparison and ablation studies. Besides CenterPoint, we compare our work with other state-of-the-art models that have either published papers or open-source code. As can be seen in Table 1, RAANet outperforms all the other models in mAP, and RAANet-lite takes the second place. For individual classes, RAANet achieves the best AP for 7 out of 10 classes, and takes the 2nd place for one of the remaining 3 classes.

4.5. Ablation Studies

In this section, we provide results of the ablation studies for components and critical parameters, which are attention module, decay factor d (for the anisotropic Gaussian mask) and λ_{aux} (weight for the density level estimation loss). The models are evaluated on nuScenes validation set. For computational efficiency, we perform all experiments in this section on ‘Car’ and ‘Pedestrian’ classes to represent large and small objects, respectively.

Anisotropic Gaussian Mask. We evaluate the performance of 2D Gaussian Mask by varying the decay factor d . The results in Fig. 5 show the variation of decay factor has lower impact on the pedestrian than the car. We set $d = 3$ and $d = 6$ for large and small objects in the main experiments.

Auxiliary Density Level Estimation Module. The AP results obtained with various weights of the loss (λ_{aux}), for the auxiliary component, are shown in Fig. 4. The loss weight values are chosen between 0.0 to 1.0. We set $\lambda_{aux} = 0.2$ for the main experiments.

Effects of different components. Tab. 2 shows the performance of the baseline as well as several types of the Range-Aware Attention Network. For RAAConv, there are four sub-components: dual branch structure, range-aware attention heatmap, initialization of range-aware kernel weights (Sec. 3.2) and learnable scalar γ (Fig. 2). The combination of those four sub-components can generate the

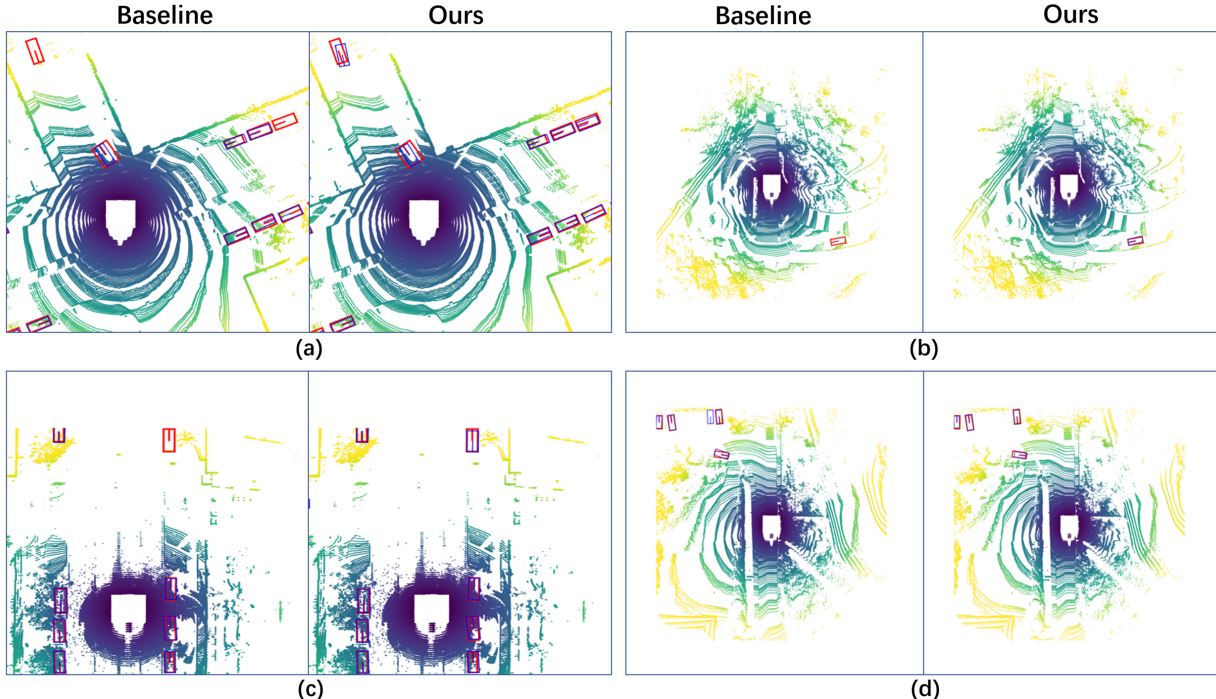


Figure 6. **Qualitative results.** (Please zoom-in for details). For each image pair, images on the left are the results inferred from the baseline, and the images on the right are the results from the proposed RAANet. Red and blue boxes denote the ground truth and predictions, respectively.

Models	RAACconv	2D Gaus.	ADLE	AP(%)	
				Car	Ped.
Baseline	X	X	X	83.98	82.80
RAANet	X	✓	X	84.32	82.82
	✓	X	X	84.43	83.61
	✓	✓	X	84.69	83.62
	✓	✓	✓	84.80	83.79

Table 3. **AP results for RAANet with PointPillar Backbone.** The baseline and comparison models are built with PointPillar proposed backbone. Comparison models are composed by various combinations of RAACconv, 2D Gaussian Mask and ADLE.

optimal gain for the RAACconv. Each aforementioned component contributes to the improvement of detection performance. It should be noticed that the pedestrian AP performance has trivial improvement with anisotropic 2D Gaussian mask. One of the probable reasons is that the annotated bbox for pedestrian class has the close width and length. This leads the anisotropic 2D Gaussian mask to fall back to original isotropic 2D Gaussian mask.

4.6. Generalizability

The proposed RAANet is further evaluated using a different backbone from PointPillars. The pillar size is set to $(0.2, 0.2)$, which follows [10]. The perception range is set to $[-51.2, 51.2] \times [-51.2, 51.2] \times [-5, 3]$. The baseline

is trained with original CenterPoint-PointPillar version. As shown in Tab. 3, our proposed RAANet still generates competitive performance using a different backbone.

4.7. Qualitative Analysis

Pairs of example outputs, obtained by the baseline and the proposed RAANet are provided in Fig. 6 for qualitative comparison. The sample data is selected from nuScenes validation dataset. In a pair, images on the left are the results inferred from the baseline, and the images on the right are the results from the proposed RAANet. It can be observed that RAANet increases true positives and suppresses false positives at the far and occluded regions. Fig. 1 in supplementary material shows more visualization examples on all-class detection results of the RAANet as well as the attention heatmaps that are generated from RAACconv.

5. Conclusion

In this paper, we have introduced the Range-Aware Attention Network (RAANet) to improve the performance of 3D object detection from LiDAR point clouds. The motivation behind the RAANet is that, in Bird's Eye View (BEV) LiDAR images, objects appear very different at various distances to the ego-vehicle, and thus, there is a need to avoid using shared-weight convolutional feature extractors. In particular, we have leveraged position and range encodings

to design a RAACconv layer with two independent convolution branches, which separately focus on sparse and dense feature extraction. Moreover, the auxiliary density level estimation module (ADLE) has been proposed to further help RAANet extract occlusion information of objects during training. Since RAACconv sets the channel number for each

branch to the half of final output channels, and ADLE is not attached during inference, the proposed RAANet is able to run in real-time. Evaluations on nuScenes dataset have shown that our proposed RAANet outperforms the SOTA works. The code is available at the following anonymous link: <https://github.com/anonymous0522/RAAN>.

References

- [1] Anonymized. Anonymized github repository for our code. <https://github.com/anonymous0522/RAAN>. 2, 6
- [2] Prarthana Bhattacharyya, Chengjie Huang, and Krzysztof Czarnecki. Sa-det3d: Self-attention based context-aware 3d object detection. *arXiv preprint arXiv:2101.02672*, 2021. 6
- [3] Holger Caesar, Varun Bankiti, Alex H. Lang, Sourabh Vora, Venice Erin Liou, Qiang Xu, Anush Krishnan, Yu Pan, Giancarlo Baldan, and Oscar Beijbom. nuscenes: A multimodal dataset for autonomous driving. *arXiv preprint arXiv:1903.11027*, 2019. 6
- [4] Qi Chen, Lin Sun, Ernest Cheung, and Alan L Yuille. Every view counts: Cross-view consistency in 3d object detection with hybrid-cylindrical-spherical voxelization. *Advances in Neural Information Processing Systems*, 2020. 6
- [5] Qi Chen, Lin Sun, Zhixin Wang, Kui Jia, and Alan Yuille. Object as hotspots: An anchor-free 3d object detection approach via firing of hotspots. In *European Conference on Computer Vision*, pages 68–84. Springer, 2020. 6
- [6] Qi Chen, Sourabh Vora, and Oscar Beijbom. Polarstream: Streaming lidar object detection and segmentation with polar pillars. *arXiv preprint arXiv:2106.07545*, 2021. 6
- [7] Xia Chen, Jianren Wang, David Held, and Martial Hebert. Panonet3d: Combining semantic and geometric understanding for lidar point cloud detection. In *2020 International Conference on 3D Vision (3DV)*, pages 753–761. IEEE, 2020. 6
- [8] MMDetection3D Contributors. MMDetection3D: Open-MMLab next-generation platform for general 3D object detection. <https://github.com/open-mmlab/mmdetection3d>, 2020. 6
- [9] Diederik P Kingma and Jimmy Ba. Adam: A method for stochastic optimization. *arXiv preprint arXiv:1412.6980*, 2014. 6
- [10] Alex H Lang, Sourabh Vora, Holger Caesar, Lubing Zhou, Jiong Yang, and Oscar Beijbom. Pointpillars: Fast encoders for object detection from point clouds. In *Proceedings of the IEEE/CVF Conference on Computer Vision and Pattern Recognition*, pages 12697–12705, 2019. 1, 2, 6, 8
- [11] Kanokphan Lertniphonphan, Satoshi Komorita, Kazuyuki Tasaka, and Hiromasa Yanagihara. 2d to 3d label propagation for object detection in point cloud. *2018 IEEE International Conference on Multimedia & Expo Workshops (ICMEW)*, pages 1–6, 2018. 6
- [12] Tsung-Yi Lin, Priya Goyal, Ross Girshick, Kaiming He, and Piotr Dollár. Focal loss for dense object detection. In *Proceedings of the IEEE international conference on computer vision*, pages 2980–2988, 2017. 4
- [13] NuScenes. NuScenes 2d object detection benchmark. <https://www.nuscenes.org/object-detection?externalData=no&mapData=no&modalities=Lidar>. 6
- [14] Adam Paszke, Sam Gross, Soumith Chintala, Gregory Chanan, Edward Yang, Zachary DeVito, Zeming Lin, Alban Desmaison, Luca Antiga, and Adam Lerer. Automatic differentiation in pytorch. 2017. 6
- [15] Meytal Rapoport-Lavie and Dan Raviv. It’s all around you: Range-guided cylindrical network for 3d object detection. In *Proceedings of the IEEE/CVF International Conference on Computer Vision*, pages 2992–3001, 2021. 6
- [16] Shaoshuai Shi, Xiaogang Wang, and Hongsheng Li. Pointrcnn: 3d object proposal generation and detection from point cloud. In *Proceedings of the IEEE Conference on Computer Vision and Pattern Recognition*, pages 770–779, 2019. 6
- [17] Shaoshuai Shi, Zhe Wang, Jianping Shi, Xiaogang Wang, and Hongsheng Li. From points to parts: 3d object detection from point cloud with part-aware and part-aggregation network. *IEEE Transactions on Pattern Analysis and Machine Intelligence*, 2020. 6
- [18] Leslie N Smith and Nicholay Topin. Super-convergence: Very fast training of neural networks using large learning rates. In *Artificial Intelligence and Machine Learning for Multi-Domain Operations Applications*, volume 11006, page 1100612. International Society for Optics and Photonics, 2019. 6
- [19] Pei Sun, Weiyue Wang, Yuning Chai, Gamaleldin Elsayed, Alex Bewley, Xiao Zhang, Cristian Sminchisescu, and Dragomir Anguelov. Rsn: Range sparse net for efficient, accurate lidar 3d object detection. In *Proceedings of the IEEE/CVF Conference on Computer Vision and Pattern Recognition*, pages 5725–5734, 2021. 5
- [20] Sourabh Vora, Alex H Lang, Bassam Helou, and Oscar Beijbom. Pointpainting: Sequential fusion for 3d object detection. In *Proceedings of the IEEE/CVF conference on computer vision and pattern recognition*, pages 4604–4612, 2020. 6
- [21] Jun Wang, Shiyi Lan, Mingfei Gao, and Larry S Davis. Info-focus: 3d object detection for autonomous driving with dynamic information modeling. In *European Conference on Computer Vision*, pages 405–420. Springer, 2020. 6
- [22] Tai Wang, Xinge Zhu, and Dahua Lin. Reconfigurable voxels: A new representation for lidar-based point clouds. *arXiv preprint arXiv:2004.02724*, 2020. 6
- [23] Tai Wang, Xinge Zhu, Jiangmiao Pang, and Dahua Lin. Probabilistic and geometric depth: Detecting objects in perspective. *arXiv preprint arXiv:2107.14160*, 2021. 6
- [24] Sanghyun Woo, Jongchan Park, Joon-Young Lee, and In So Kweon. Cbam: Convolutional block attention module. In *Proceedings of the European conference on computer vision (ECCV)*, pages 3–19, 2018. 3
- [25] Peixi Xiong, Xuetao Hao, Yunming Shao, and Jerry Yu. Adaptive attention model for lidar instance segmentation. In *Advances in Visual Computing*, pages 141–155. Springer International Publishing, 2019. 1
- [26] Yan Yan, Yuxing Mao, and Bo Li. Second: Sparsely embedded convolutional detection. *Sensors*, 18(10):3337, 2018. 2
- [27] Bin Yang, Wenjie Luo, and Raquel Urtasun. Pixor: Real-time 3d object detection from point clouds. In *Proceedings of the IEEE conference on Computer Vision and Pattern Recognition*, pages 7652–7660, 2018. 2
- [28] Yangyang Ye, Houjin Chen, Chi Zhang, Xiaoli Hao, and Zhaoxiang Zhang. SarpNet: Shape attention regional proposal network for lidar-based 3d object detection. *Neurocomputing*, 379:53–63, 2020. 6

- [29] Tianwei Yin, Xingyi Zhou, and Philipp Krähenbühl. Center-based 3d object detection and tracking. *CVPR*, 2021. [3](#), [6](#), [7](#)
- [30] Han Zhang, Ian Goodfellow, Dimitris Metaxas, and Augustus Odena. Self-attention generative adversarial networks. In *International conference on machine learning*, pages 7354–7363. PMLR, 2019. [4](#)
- [31] Xingyi Zhou, Dequan Wang, and Philipp Krähenbühl. Objects as points. In *arXiv preprint arXiv:1904.07850*, 2019. [3](#), [4](#)
- [32] Yin Zhou, Pei Sun, Yu Zhang, Dragomir Anguelov, Jiyang Gao, Tom Ouyang, James Guo, Jiquan Ngiam, and Vijay Vasudevan. End-to-end multi-view fusion for 3d object detection in lidar point clouds. In *Conference on Robot Learning*, pages 923–932. PMLR, 2020. [1](#)
- [33] Yin Zhou and Oncel Tuzel. Voxelnet: End-to-end learning for point cloud based 3d object detection. In *Proceedings of the IEEE conference on computer vision and pattern recognition*, pages 4490–4499, 2018. [1](#), [2](#)
- [34] Benjin Zhu, Zhengkai Jiang, Xiangxin Zhou, Zeming Li, and Gang Yu. Class-balanced grouping and sampling for point cloud 3d object detection. *arXiv preprint arXiv:1908.09492*, 2019. [6](#)
- [35] Xinge Zhu, Yuexin Ma, Tai Wang, Yan Xu, Jianping Shi, and Dahua Lin. Ssn: Shape signature networks for multi-class object detection from point clouds. In *Computer Vision-ECCV 2020: 16th European Conference, Glasgow, UK, August 23–28, 2020, Proceedings, Part XXV 16*, pages 581–597. Springer, 2020. [6](#)